Transmission of Solar Radiation by Clouds over Snow and Ice Surfaces. Part II: Cloud Optical Depth and Shortwave Radiative Forcing from Pyranometer Measurements in the Southern Ocean

MELANIE F. FITZPATRICK

Department of Earth and Space Sciences, University of Washington, Seattle, Washington

STEPHEN G. WARREN

Department of Earth and Space Sciences, and Department of Atmospheric Sciences, University of Washington, Seattle, Washington

(Manuscript received 16 August 2004, in final form 3 June 2005)

ABSTRACT

Downward solar irradiance at the sea surface, measured on several voyages of an icebreaker in the Southern Ocean, is used to infer transmittance of solar radiation by clouds. Together with surface albedo estimated from coincident hourly sea ice reports, instantaneous cloud radiative forcing and effective cloud optical depth are obtained. Values of "raw cloud transmittance" (trc), the ratio of downward irradiance under cloud to downward irradiance measured under clear sky, vary from 0.1 to 1.0. Over sea ice, few values of trc were observed between 0.8 and 1.0, possibly due to the threshold nature of the aerosol-to-cloud-droplet transition. This sparsely populated region of transmittances is referred to as the Köhler gap.

The instantaneous downward shortwave cloud radiative forcing is computed, as well as the time-averaged net forcing. The net forcing at a solar zenith angle of 60° is typically -250 W m^{-2} over open ocean, but only half this value over sea ice because of the higher surface albedo and less frequent occurrence of clouds.

"Effective" optical depths τ (for a radiatively equivalent horizontally homogeneous cloud) are classified by season and surface type. The frequency distributions of τ are well fitted by decaying exponentials, giving a characteristic optical depth of 15 at 47°S, increasing to 24 in the region of maximum cloud cover at 58°S, and decreasing to 11 at 67°S near the coast of Antarctica.

1. Introduction

In Fitzpatrick et al. (2004, hereafter Part I), a method was developed to infer cloud information from measurements of downward broadband solar irradiance using pyranometers. The observed "raw" cloud transmittance (trc) is used, together with knowledge of the solar zenith angle θ and an estimate of surface albedo α, to infer an inherent property of the cloud field, called the "effective" optical depth τ. This derived quantity is designed to be useful in climate studies (together with regional climatologies of cloud cover and surface albedo) for computing the solar transmittance over other surface types and at other zenith angles. Such an effective optical depth has been used previously, for example, by Barker et al. (1998). In Part I a parameterization was developed for trc as a function of τ, θ, and α, by fitting simple functions to the results of a multilayer multispectral atmospheric radiative transfer model, using for the surface boundary conditions the spectral shapes of albedo for snow, ice, and water. Over high-albedo surfaces, multiple reflection between the cloud and the ground enhances the observed downward irradiance (e.g., Nichol et al. 2003); this is taken into account in the parameterization. The parameterization for trc was shown to give rms errors of only 1%–2% when compared to the trc computed by the radiative transfer model. Although the effective droplet size cannot be obtained from a single broadband measurement, lack of knowledge of the droplet sizes causes little error in computed trc (typically 2%) when the inferred τ is applied to other environments of θ and α.

In this paper we use the parameterization to analyze pyranometer data from several ship voyages in the Southern Ocean.

Corresponding author address: Melanie F. Fitzpatrick, Earth and Space Sciences, University of Washington, Box 351310, Seattle, WA 98195.
E-mail: fitz@atmos.washington.edu

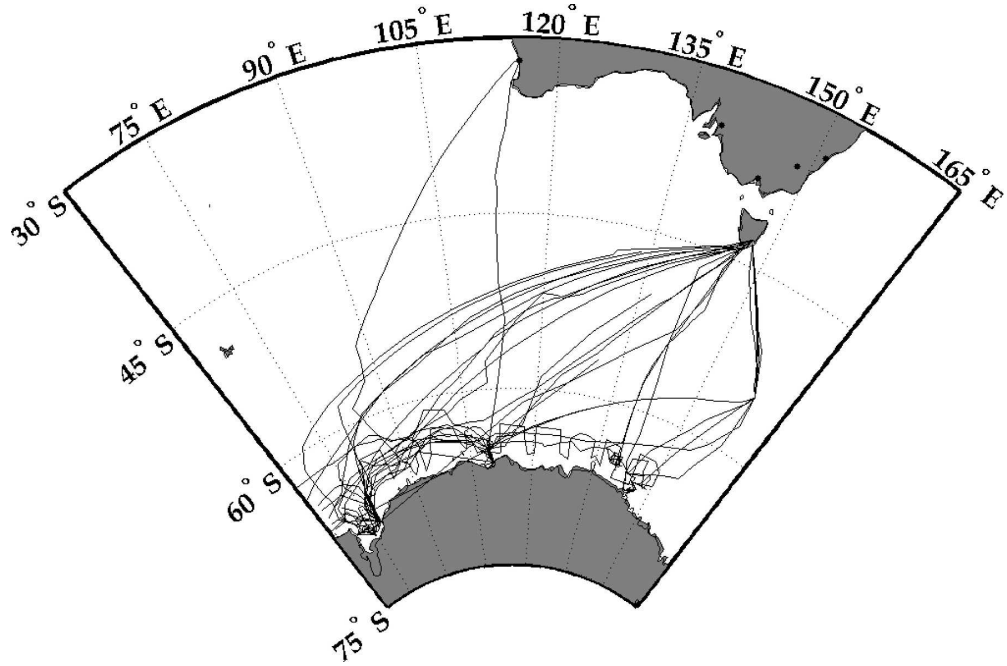

FIG. 1. Tracks of the RSV *Aurora Australis* voyages used in the analysis of cloud optical properties (sections 3 and 4). Voyages were confined to the Southern Ocean and East Antarctic region between 43° and 69°S, 55° and 159°E.

2. Voyage data

Data were collected on voyages of the RSV *Aurora Australis* as part of the Australian National Antarctic Research Expeditions (ANARE) during the years from 1991 to 2002. Voyages were carried out between latitudes 43° and 69°S, longitudes 55° and 159°E. Voyage duration varied from 4 to 12 weeks, covering winter, spring, and summer seasons. The tracks of 18 voyages for which we determine cloud properties (in sections 3 and 4) are shown in Fig. 1. We selected voyages that provided observations of ice conditions and weather, coincident with instrumental measurements of solar irradiance.

Considerable variation in seasonal sea ice cover occurs among these voyages. Hourly visual observations were recorded, including estimates of the fractional coverage of the ocean surface for each of several ice types within 2 km of the ship, as well as the ice thickness and the snow cover thickness. Standard observational procedures were used according to the protocol of the Antarctic Sea Ice Processes and Climate Program (ASPeCt), given by Worby (1999). Together with surface albedos of different types of Antarctic sea ice, which have been measured in situ by Allison et al. (1993) and Brandt et al. (2005), these hourly observations are used to determine the area-averaged surface albedo at a particular location. Figure 2 shows the seasonal variation of broadband surface albedo α within the sea ice zone, with representative albedo distributions. In the winter, albedos are slightly higher (with a mode of 0.75) and indicate less thin ice and open water than in the spring and summer when albedos range from 0.2 to 0.8 with a mode of 0.65. This transitional period in spring and summer, characterized by decaying ice and brash and hence larger areas of open water, results generally in a greater frequency of lower surface albedos. Visual ice-type distributions are estimated to be accurate to within one-tenth of sea ice concentration (A. Worby 2001, personal communication). We estimate that surface albedos derived from these reports are typically uncertain to ± 0.06 in albedo (Fitzpatrick et al. 2004). The largest source of error in the inference of inherent cloud properties (section 4) is uncertainty in surface albedo.

On most voyages between 1991 and 2002, cloud amount and type were recorded at 3-hourly intervals by trained weather observers. We obtained cloud observations for these voyages both from the Comprehensive Ocean–Atmosphere Data Set (COADS) (Woodruff et al. 1998) and from the archives of the Commonwealth Bureau of Meteorology. Comparison of winter, spring, and summer voyages shows little seasonal variation in total cloud cover and low cloud amount (Fig. 3). Typically, the Southern Ocean region displays average total cloud exceeding 80% (Warren et al. 1988, Maps 6–9), well above the global average of 64% (Hahn et al.

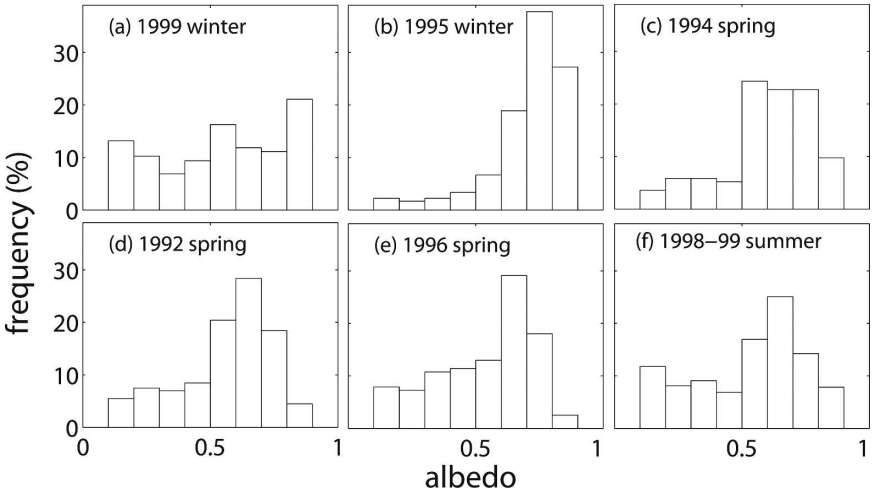

FIG. 2. Distribution of surface albedos in the East Antarctic sea ice zone in different seasons, excluding regions with no ice cover. Area-averaged surface albedos for a particular location are determined from measured surface albedos for different ice types (Brandt et al. 2005), together with hourly visual observations of each of these ice types including estimates of the fractional coverage of the ocean surface, the ice thickness, and the snow cover thickness. Plots are arranged according to chronological dates within a season with (a) being earliest dates to (f) being latest.

1995). Cloud types for the same voyages show slight seasonal differences. Figure 4a shows the frequency distribution of cloud types in the sea ice zone, while Fig. 4b shows those over open ocean. High and middle clouds, which are dominated by cirrus and altocumulus respectively, show little variation with season. Low cloud displays some changes in summer in the sea ice zone, with an increase in clear sky and a slight decrease in the frequency of cumulus and stratus clouds compared to winter. The cumulus in winter are probably due to convection over leads, where the air–sea temperature gradient is large and unstable. Comparing Figs. 4a and 4b, slightly more clear sky is reported over sea ice than over open ocean.

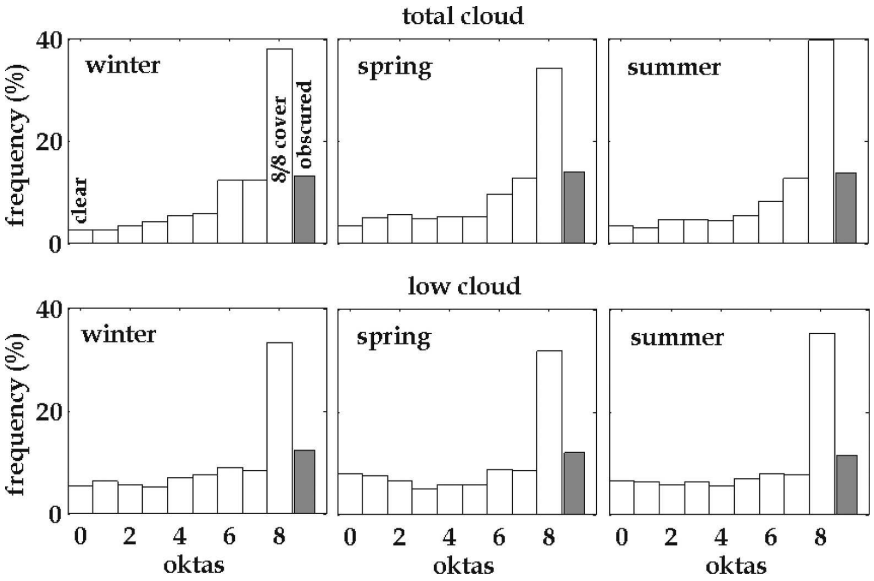

FIG. 3. Frequency of cloud amounts in oktas (eighths) observed during voyages of *Aurora Australis* for the period 1990–95. The code value 9 means "sky obscured," usually due to fog.

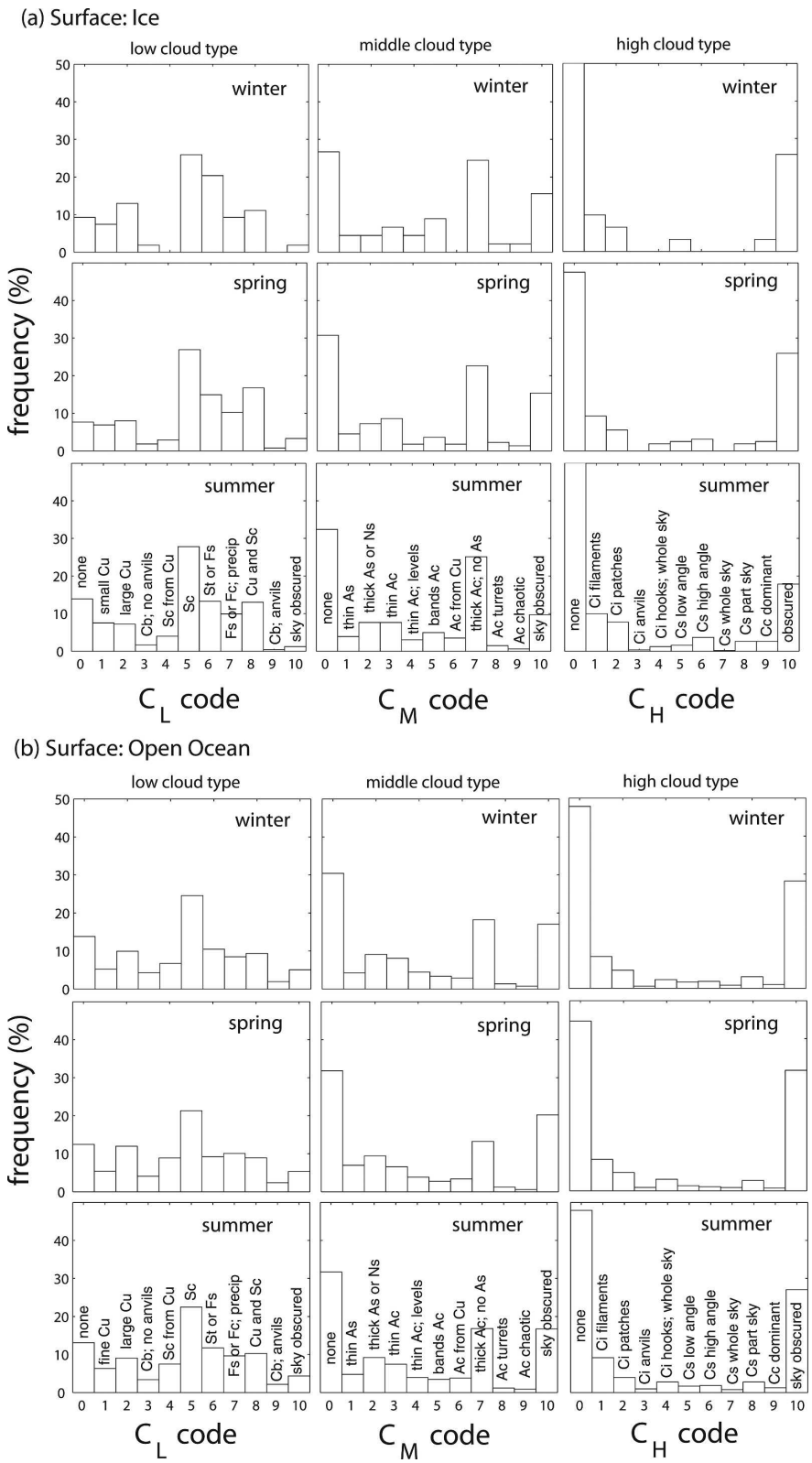

FIG. 4. Frequencies of cloud types observed during voyages of *Aurora Australis* for the period 1990–95 (a) within the sea ice zone and (b) in the open ocean. For a legend of cloud-type abbreviations used in this figure, see Table 1. The complete specifications of the cloud-type code values are given by WMO (1956).

TABLE 1. Cloud type abbreviations used for surface weather observations of clouds in Fig. 4. More detail is given by WMO (1956).

Ac	Altocumulus	Cu	Cumulus
As	Altostratus	Fc	Fractocumulus
Cb	Cumulonimbus	Fs	Fractostratus
Cc	Cirrocumulus	Ns	Nimbostratus
Ci	Cirrus	Sc	Stratocumulus
Cs	Cirrostratus	St	Stratus

In addition to observations of sea ice and cloud conditions, solar irradiance measurements covering the spectral range 0.3–2.8 μm were obtained from the same research vessel, the RSV *Aurora Australis*, over the same period 1991–2002 (obtained from the Australian Antarctic Division Data Center). Standard "precision spectral pyranometers" (PSPs) from the Eppley Corporation, mounted on gimbals on opposite sides of the ship, measured downwelling irradiance at 10-s intervals for the duration of each voyage. The pyranometers were cleaned daily and calibrated annually. However, absolute calibration is not necessary for our purpose, as explained below. The use of dual instruments enables corrections due to shadowing and tilt. Figure 5 shows a typical record over five consecutive days, for 10-min averages of solar irradiance. In our analyses, we do not use measurements at $\theta > 80°$ because the instrument's deviation from cosine response is greater at large θ and errors caused by slight tilt of the instruments are also larger at large θ. Ambrosetti et al. (1986) estimate errors of the Eppley PSP due to azimuth, cosine response, instrument drift, tilt errors, and calibration to be on the order of $\pm 3\%$.

The hemispheric field of view of the instruments is shown in Fig. 6, as photographed by an all-sky camera mounted next to one of the pyranometers. To account for the black ship structures obscuring the field of view and decreasing the all-sky irradiance, a correction of 3.3% is applied to the irradiance measurements. This correction was determined by digitizing the image and applying an equal-area projection template to estimate the obstruction of the instrument's field of view (after Henderson-Sellers and McGuffie 1988).

3. Observed radiative effects of clouds

Some cloud radiative properties can be obtained simply by using these pyranometer measurements. Our method for obtaining cloud properties is described by Fitzpatrick et al. (2004). It makes use of methods developed by Leontyeva and Stamnes (1994) and Lubin and Simpson (1997); it differs from theirs in that we do not compute the clear-sky transmittance using a radiative transfer model, but rather obtain it from observation. Raw cloud transmittance (trc*)* is obtained as the ratio of the measured downwelling irradiance to the downwelling irradiance measured under a clear sky for the same solar zenith angle. The cloud field may be inhomogeneous and even patchy. The clear-sky transmittance is shown in Fig. 7. These are measured values of downward irradiance under clear sky divided by the extraterrestrial solar irradiance, $Q\cos\theta$, where Q is the solar constant adjusted for variation of the earth–sun distance. The points plotted in Fig. 7 are measurements at times that the ship's meteorologists reported clear sky, for the voyage of September–November 1996. There is more scatter for $\theta > 75°$ because tilting of the pyranometer causes larger error when the sun is low. In addition, a low sun results in higher surface albedos. This may explain the slight upturn in clear transmittance at large solar zenith angles. There are no values for $\theta < 50°$ because clear sky was not reported on this

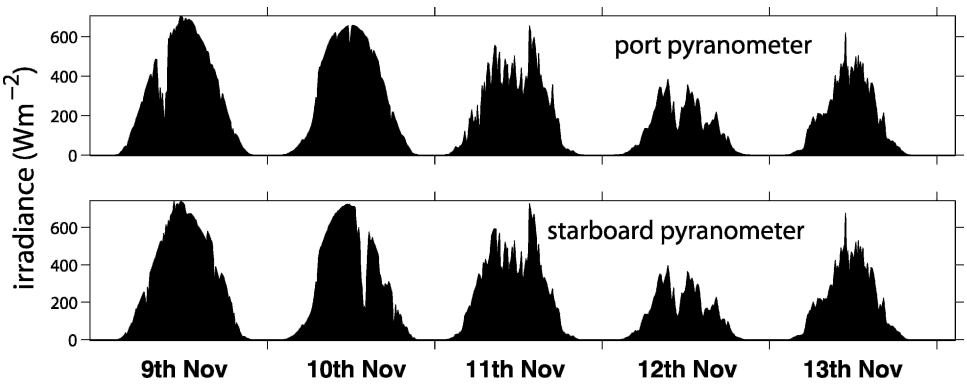

FIG. 5. Time series of irradiance measurements over a 5-day period, from two gimbaled broadband (0.3–2.8 μm) pyranometers permanently mounted on opposite sides of the *Aurora Australis*. Comparison of simultaneous records from these two instruments allows testing for errors due to shadowing and tilt.

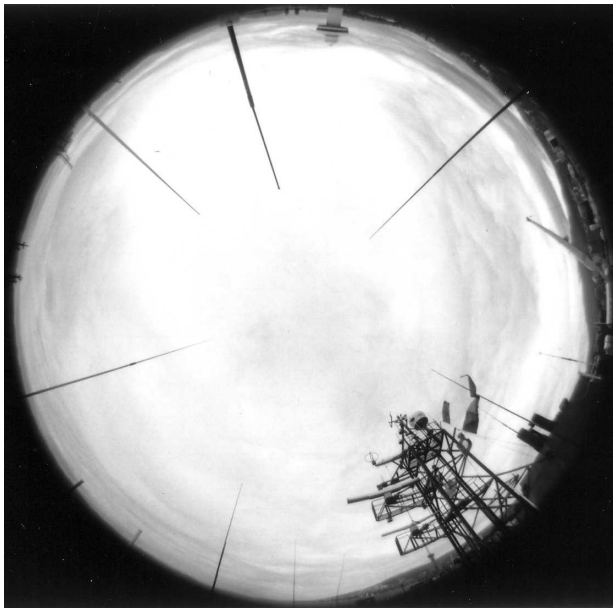

FIG. 6. The field of view of a pyranometer mounted on the upper deck of the *Aurora Australis*. Obstruction of the sky by the black ship structures decreases the irradiance measurements by approximately 3.3%. The photograph is from an all-sky camera mounted next to the pyranometer.

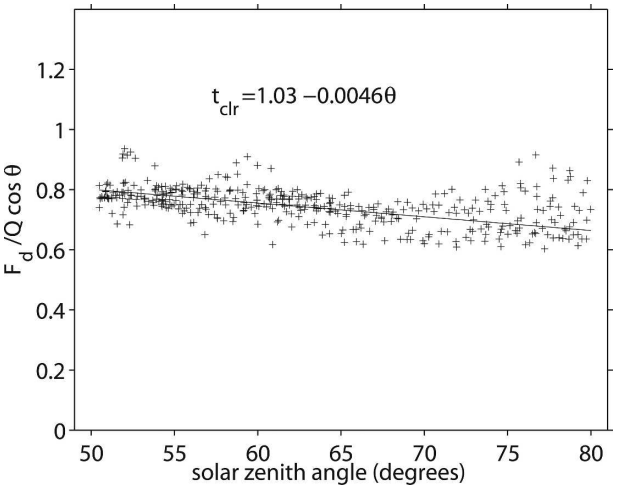

FIG. 7. Clear-sky transmittance as a function of solar zenith angle. The downward irradiance measured by the pyranometers, F_d, is divided by the extraterrrestrial solar irradiance, $Q \cos\theta$. Values are plotted for all times that the shipboard meteorologists reported clear sky on the 1996 springtime voyage. The linear fit shown is used to obtain trc in Fig. 8.

voyage while the ship was passing through the lower-latitude parts of the ocean (43°–50°S). The clear-sky transmittance shows a slight decline with θ, which we fit with a straight line.

To obtain trc, each pyranometer measurement (of the downward flux from the entire sky hemisphere of 2π steradians) is divided by the clear-sky flux for the corresponding solar zenith angle shown in Fig. 7. An advantage of using measurements rather than model calculations to determine the clear-sky transmittance is that it does not require absolute calibration of the pyranometer, it avoids modeling errors, and takes into consideration the mean aerosol effect.

If instantaneous measurements are used, in the case of scattered or broken clouds there are two classes of observations: the pyranometer is either in the shadow of a cloud or in direct sunlight. In the latter case, the sun is temporarily between clouds and the measured downward irradiance equals (or even exceeds) the clear-sky value, so trc ≈ 1.0 and the CRF is zero for this instantaneous measurement. In the former case, that is, when a cloud comes in front of the sun, the observed downward irradiance is about the same as it would be for an overcast cloud of the same optical thickness because almost all of the irradiance incident on the cloud top from above comes directly from the sun, not from the sky. So instantaneous measurements would represent either clear sky or overcast cloud, even when the cloud field is patchy.

The basic data recorded on the ships were 10-s averages, that is, nearly instantaneous, but most of the data available to us had been averaged up to 10-min averages. In the case of scattered or broken clouds, the time average therefore means that during these 10 min the pyranometer might be at times shaded by clouds and at other times in direct sunlight. As the averaging time increases, the frequency distribution of trc values must therefore change. However, significant change apparently happens only for averaging times longer than 10 min. Although most of our data are 10-min averages, for one voyage we do have spot readings of 10-s duration taken every 10 min, and the frequency distribution of trc from these readings (for all times during the voyage that the ship was in ice) is very similar to the frequency distribution of trc from the 10-min averages. The 10-min and 10-s histograms also resembled each other for the observations in open ocean.

We therefore tried increasing the averaging time to watch the histogram evolve. It was nearly unchanged out to 80 min; then its shape began to change, and when the averaging time reached 200 min the original pattern disappeared. We therefore think that the results presented here, based on 10-min averages, are representative of instantaneous measurements. All of our plots include both clear (trc ≈ 1) and cloudy (trc < 1) scenes, so a monthly averaged cloud transmittance can be obtained simply by averaging all individual values of trc.

Figure 8 shows trc for this same voyage in 1996. The

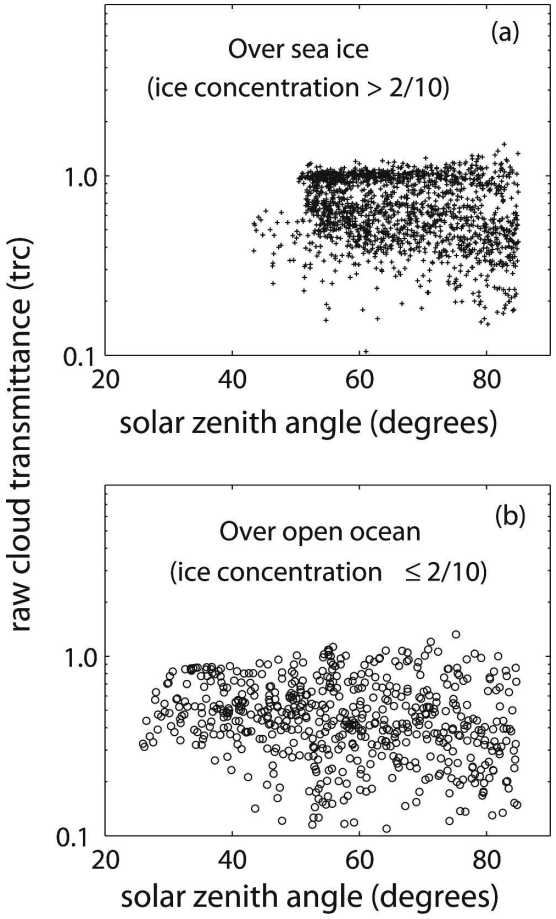

FIG. 8. The 10-min averages of "raw" cloud transmittance (the ratio of downward irradiance under cloud to downward irradiance measured under clear sky at the same solar zenith angle) for the 1996 springtime voyage over (a) sea ice (where the concentration of sea ice exceeds 0.2) and (b) open ocean (where the concentration of sea ice is at most 0.2).

data are separated into two classes of surface type: open water, where the areal concentration of ice is at most 0.2, and sea ice, where the areal concentration of ice is greater than 0.2. The range of trc values is similar to that shown for the Arctic Ocean in summer by Lubin and Simpson (1997, their Fig. 2). Figure 8 shows that clear sky (the band of points along the top) is more common over sea ice than over open ocean. The presence of sea ice prevents the exchange of heat and moisture between the ocean and atmosphere. Under cloudy sky in the sea ice zone, trc is greater than over the open ocean principally because of multiple reflections over the higher surface albedo. It is also apparent that transmittance in the sea ice zone through even the thinnest clouds was usually 20% less than that of clear sky. We have named this sparsely populated region of observed transmittances the Köhler gap (trc ~0.8 in Fig. 8a) with the idea that it may be due to the threshold nature of the aerosol-to-cloud-droplet transition (Rogers 1979, chapter 5). Such a gap would not be expected if a great variety of aerosol types were active as cloud condensation nuclei; its appearance in these data may be an indication of the very clean air in this remote part of the ocean. However, a Köhler gap also appears to be present in the Arctic summer between Svalbard and North Greenland (Minnett 1999, his Fig. 3). Figure 9 shows a histogram of the same transmittance values with the Köhler gap evident. Some values of trc exceed 1.0. Such values may occur under clear sky due to imperfect leveling of the pyranometers and under cloudy sky when the solar beam passes between clouds causing the downward solar irradiance to exceed the clear-sky irradiance. The various sky conditions that can cause trc > 1 are discussed in detail by Pfister et al. (2003), who also provide a review of the literature on this topic.

The effect of clouds on the radiation budget is normally called cloud radiative forcing (CRF), although it might more accurately be referred to as cloud radiative

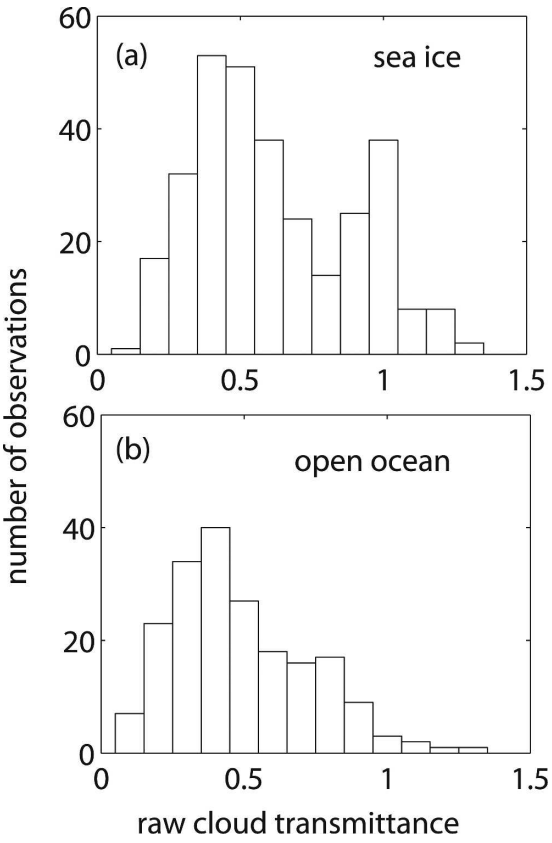

FIG. 9. Frequency distribution of raw cloud transmittance values (trc), showing (a) a bimodal distribution over sea ice and (b) a monomodal distribution over open ocean. Data are from the 1996 springtime voyage.

effect, since "forcing" in other contexts means changes in radiative fluxes (due to an external influence on the system, often specifically anthropogenic contributions) rather than the climatological baseline. Clouds are of course highly interactive with the other components of the climate system. Here we use the standard term, CRF. In the solar (shortwave) spectrum, clouds generally have a cooling effect due to the reflection of sunlight back to space, so CRF is negative. However, the magnitude of this cooling in the shortwave depends on the albedo contrast of the cloud with the surface. In this paper we derive cloud radiative forcing only at the surface, and only the shortwave forcing. The reduction in downward shortwave irradiance relative to clear sky we call downward shortwave cloud radiative forcing, CRF_d, which is plotted in Fig. 10 versus solar zenith angle (a) over sea ice and (b) over open ocean. Each data point represents a 10-min average for the duration

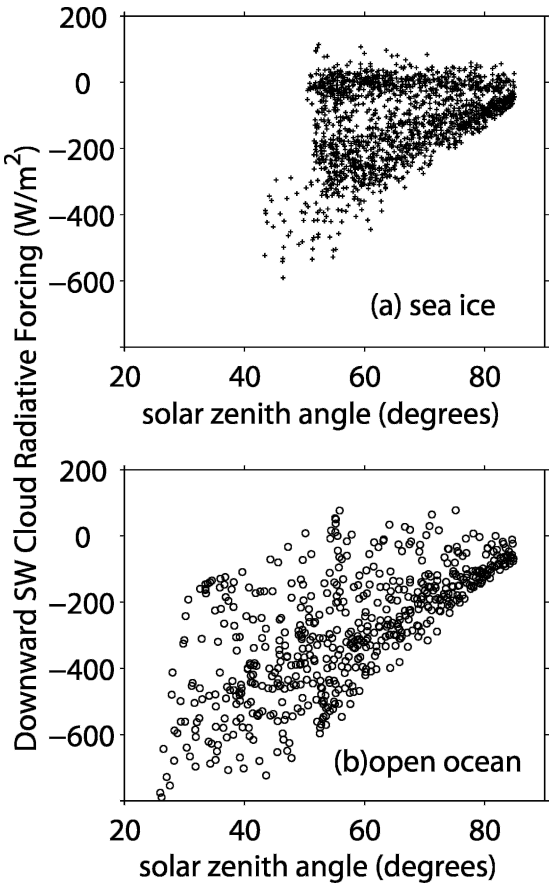

FIG. 10. Instantaneous values of downward shortwave cloud radiative forcing (the reduction in downward shortwave irradiance) at the surface as a function of solar zenith angle over (a) sea ice and (b) open ocean. Values shown are 10-min averages for the 1996 springtime voyage. The more frequent occurrence of clear sky over sea ice than over open ocean is apparent.

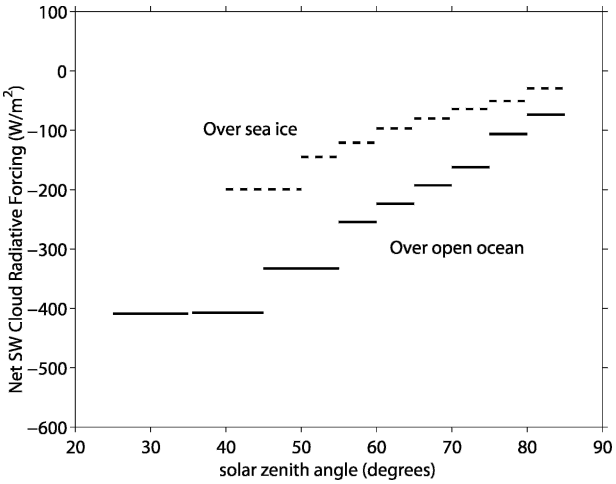

FIG. 11. Net shortwave cloud radiative forcing (CRF_n) at the surface obtained by multiplying the downward shortwave cloud radiative forcing by $(1 - \alpha)$, where α is the surface albedo. Each average (for a solar-zenith-angle bin) is the difference in net shortwave irradiance between all conditions and clear conditions. Data are from the 1996 spring voyage. CRF_n is smaller over sea ice due to both the higher surface albedo and the less frequent occurrence of clouds.

of a single voyage. The more frequent occurrence of clear sky over sea ice than over open ocean is again evident. The net shortwave cloud radiative forcing (CRF_n) at the surface, shown in Fig. 11 for the same voyage, is obtained by multiplying CRF_d by $(1 - \alpha)$. CRF_n is of smaller magnitude over sea ice due to both the higher surface albedo and the less frequent occurrence of clouds. Each average for a solar-zenith-angle bin in Fig. 11 is the difference in net shortwave irradiance at the surface between all conditions and clear conditions.

4. Inherent cloud properties

The transmittance and CRF shown in Figs. 8–11 are not inherent properties of the clouds. They depend upon the local conditions of surface albedo and solar zenith angle when the measurement was made. To use these data to generalize the results for a study of the radiation budget of the Southern Ocean, we need to infer an inherent property of the cloud field, which is independent of solar zenith angle and local surface albedo. We choose the property of "effective" cloud optical depth τ, as presented in Fitzpatrick et al. (2004). Effective cloud optical depth was determined using a simple parameterization that relates cloud transmittance (trc) to cloud optical depth τ, surface albedo α, and solar zenith angle θ. The parameterization, motivated by Wiscombe (1975) and derived using a multilevel spectral radiative transfer model, is

$$\mathrm{trc} = \frac{a(\tau) + b(\tau)\cos\theta}{1 + (c - d\alpha)\tau}. \quad (1)$$

For an explanation of the physical reasoning behind this parameterization and its development, and discussion of the coefficients, see Fitzpatrick et al. (2004). The coefficients were determined using three solar zenith angles ($\cos\theta = 0.2, 0.4, 0.6$), 14 cloud optical depths (τ from 0.02 to 88 with geometric spacing, and $\tau = 0$ for clear sky), and 12 different surface albedos from 0.09 to 0.87. To make the parameterization accurate in the limit of $\tau \to 0$, we found it necessary to make the coefficients a and b functions of τ. Values of these coefficients are given by Fitzpatrick et al. (2004, Table 1). In the present study, we use the broadband coefficients covering the same wavelength region as the pyranometer. The parameterization faithfully mimics the results of the radiative transfer model used in its development, with rms errors of 1%–2%.

We now apply the parameterization to data from all of the voyage tracks in Fig. 1, which includes not only voyages with hourly ice observations but also additional voyages carried out in the Southern Ocean (and not in the sea ice zone) between 1991 and 2002. Voyages without ice reports can still be used in the open-ocean part of their routes because the surface albedo of ocean water can be assumed constant. The nonlinear equation (1) is solved for cloud optical depth using a least squares method (Press et al. 1992, 678–683). Figure 12 shows the distributions of effective cloud optical depth (separate histograms for the sea ice zone and the open ocean) during the different seasons. This optical depth is "effective" in that it is calculated assuming a horizontally homogeneous overcast cloud and the cloud is assumed to consist of liquid water droplets with a standard effective radius of 8.6 μm. As discussed in Fitzpatrick et al. (2004), we use this optical depth as an intermediate quantity whose utility is determined by its ability to predict the transmittance of the observed cloud field over surfaces and under illumination different from those observed. Here, we present these effective cloud optical depths and note that the absolute values can be in error as much as 50% due to cloud inhomogeneity (Boers et al. 2000).

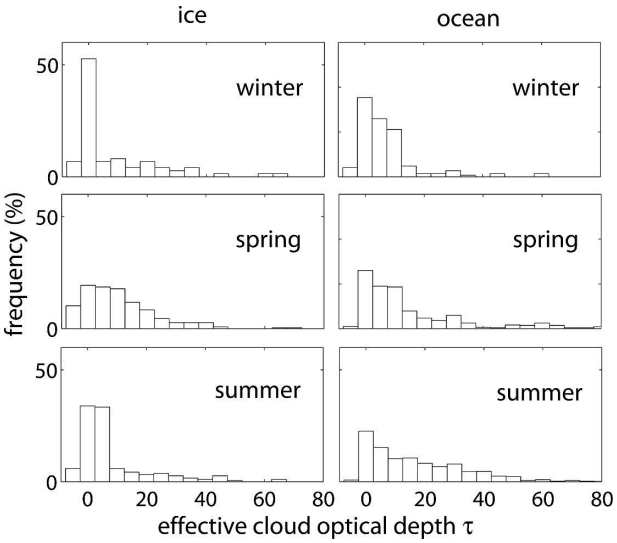

FIG. 12. Frequency distribution of effective cloud optical depth over ice and ocean surfaces for different seasons. Data are from voyages between the years 1991 and 2002 for which concurrent observations of ocean, sea ice, and cloud conditions were available.

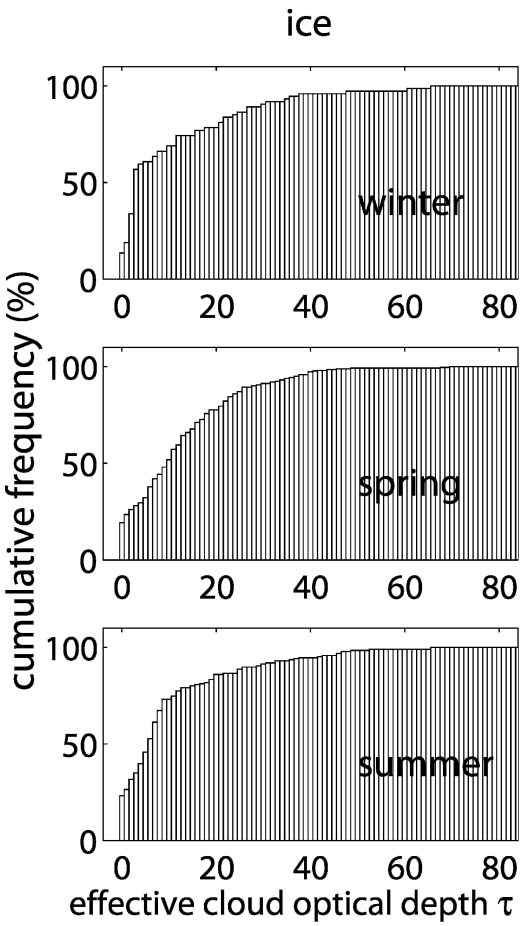

FIG. 13. Cumulative frequency distribution of effective cloud optical depth over ice surfaces for the same voyages of the *Aurora Australis* used in Fig. 12. Bin size has been reduced to one unit of optical depth with all negative values included in the zero bin. The concavity of the curve suggests that there is a transition between clear sky and cloudy sky identified earlier as the "Köhler gap."

Observed effective radii for springtime cloud droplets in the Southern Ocean range from 4.5 to 16.6 μm (Boers and Krummel 1998). They were measured be-

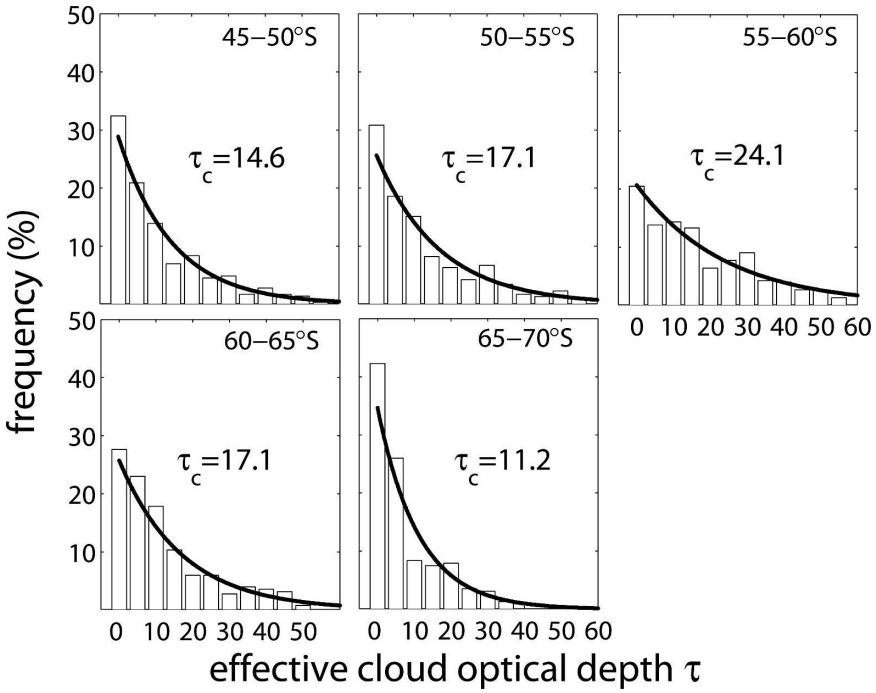

FIG. 14. Cloud optical depth for different latitude intervals for all voyages of the *Aurora Australis* between 1991 and 2002 with concurrent observations of ocean, sea ice, and cloud conditions. The observations include all seasons and as such are biased toward spring and summer when a greater number of voyages occurred. The number of observations for each season and each latitude interval are shown in Table 2. Exponential fits are also given, where $f(\tau) = \tau_c^{-1} \exp(-\tau/\tau_c)$. The values shown in the figure are percentages for bins of width $\Delta\tau = 5$.

tween 40° and 55°S during the First Aerosol Characterization Experiment (ACE-1), in November and December 1995. No trend was observed in r_{eff} within this latitude range, so these values may also be representative for other parts of the Southern Ocean (R. Boers 2000, personal communication). However, r_{eff} is probably smaller in summer than in winter because there are more cloud condensation nuclei in summer (Ayers and Gras 1991).

As stated above, we use cloud optical depth as a convenient intermediate quantity to predict the cloud radiative effects. However, it is still interesting to consider how the effective optical depths vary seasonally and with the different underlying surfaces. We first classify the optical depth distributions by season and surface type. Figure 12 shows that in winter and summer there is far more clear sky and optically thin cloud over sea ice than over open ocean. In springtime there is less difference in the optical depth distributions over ice and water for unknown reasons. The Köhler gap is not apparent in Fig. 12, perhaps because the bin size is too large. In Fig. 13 we therefore show the *cumulative* frequency distribution of cloud optical depth over ice surfaces for these same voyages using a smaller bin size than in the previous figure. The concave-upward shape of the curve at small optical depths may represent the Köhler gap.

In Fig. 14 we show frequency distributions of effective cloud optical depth classified not by season and surface type but rather by latitude. Values of optical depth range as high as 60, with greater optical depths occurring over open water north of the sea ice edge, which in the East Antarctic longitudes moves seasonally between approximately 61° and 66°S (maximum ice

TABLE 2. Number of observations used in the analysis for cloud optical depth and cloud cover (Figs. 13 and 14) for different latitude intervals in different seasons.

Latitude band (°S)	Total	Winter	Spring	Summer	Autumn	Approx ratio
45–50	797	79	292	337	89	1:3:4:1
50–55	528	37	207	241	43	1:5:6:1
55–60	380	28	114	201	37	1:3:5:1
60–65	268	19	162	83	4	1:8:4:0
65–70	254	53	100	101	0	1:2:2:0

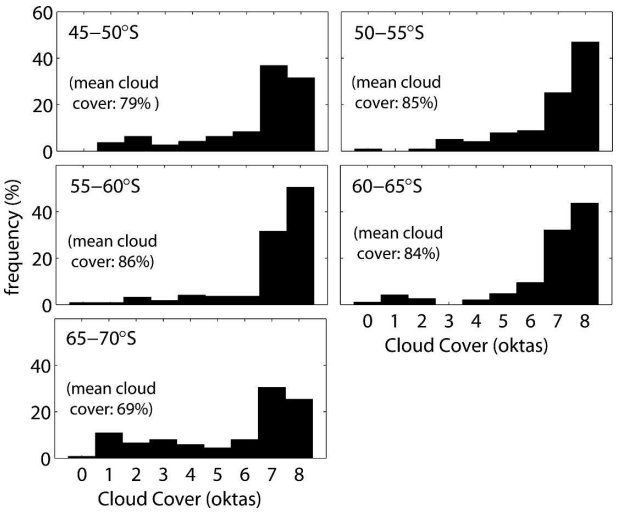

FIG. 15. Frequency distribution of reported cloud cover for different latitude intervals from observations made on the same voyages of the *Aurora Australis* used in Fig. 12. The mean cloud cover is also given. Code 9 values denoting fog were included with code 8 values denoting total cloud cover (see Fig. 3).

extent in September, minimum in February). Clear sky and thin cloud are twice as common in the 65°–70°S latitude band close to the Antarctic continent as in the 55–60°S band that lies just outside the sea ice zone.

The histograms of optical depth in Fig. 14 can be fitted approximately with simple functions, which may be useful for climate modeling and analyses. This is done in Fig. 15, fitting an exponential decay function to the data from each latitude band:

$$f(\tau) = \frac{1}{\tau_c} \exp(-\tau/\tau_c), \tag{2}$$

where τ_c is a characteristic optical depth whose frequency of occurrence is a factor of e below that for $\tau = 0$. This characteristic optical depth is also the average optical depth, if the exponential distribution is accurate. This function is a good representation of the histograms; it exhibits errors of up to 3% for $\tau > 5$, and up to 9% for $\tau < 5$. An alternative fit was tried using a delta function for clear sky and small optical depths and an exponential decay function for the larger optical depths, but this proved less accurate.

The thickest clouds are found at 55°–60°S, slightly north of the peak of zonal average cloud cover (Fig. 6.3 of van Loon 1972; Fig. 10 of Warren et al. 1988), and τ_c decreases both to the north and south. Our value of $\tau_c = 17$ for the 60°–65°S latitude zone appears to match the frequency distribution of τ obtained by Ricchiazzi et al. (1995) for Palmer Station on the west side of the Antarctic Peninsula at 64°S in this same latitude zone. Over the interior of Antarctica, clouds are of course much thinner, with $\tau_c \approx 1$ (Mahesh et al. 2001 Fig. 10). The optical depth distributions for midlatitude continental clouds over Canada were better fit to Γ distributions than to exponentials (Barker et al. 1998), as they showed a modal τ of 10–20, perhaps indicating a Köhler gap for $\tau < 10$. In Fig. 14 the Köhler gap is less distinct due to our choice of bin size. A smaller bin size makes the gap more obvious but increases the noise in the histogram.

Observed cloud cover for these same voyages and same latitude bands is shown in Fig. 15. This figure also shows that overcast cloud is less frequent close to the Antarctic continent than farther out in the ocean. A comparison of average cloud cover for different latitude bands gives 69% for the 65°–70°S band, compared with 86% for the 55°–60°S band. We also tried to classify the τ histograms by cloud type (grouping the 27 cloud types of Fig. 4 into nine groups), but there were insufficient observations of each type to obtain statistically reliable results.

5. Conclusions and future work

The parameterization developed in Part I (Fitzpatrick et al. 2004) relating raw cloud transmittance trc to cloud optical depth τ, surface albedo α, and solar zenith angle θ was applied to the pyranometer measurements during several voyages of the RSV *Aurora Australis* in the Southern Ocean between 1991 and 2002. Seasonal and latitudinal distributions of effective cloud optical depth are presented. The effective optical depth we derive is only a convenient intermediate quantity, not an end in itself. We envision using it to extend the dataset seasonally and geographically. Using the parameterization of Eq. (1), one can compute what the transmittance of this same cloud field would be under different conditions of solar illumination and surface albedo, to obtain diurnal and seasonal cycles of cloud radiative forcing. The distributions of cloud optical depth from this paper, and surface albedo from Brandt et al. (2005), can be combined to give values of transmittance for different solar zenith angles in different seasons. The resulting cloud transmittance estimates can then be used together with cloud-type distributions reported over the Southern Ocean to estimate the geographical variation of shortwave cloud radiative forcing in the ocean around Antarctica.

Acknowledgments. We thank Ian Allison of the Australian Antarctic Division for sponsoring the field work for this project, and Richard Brandt, Tom Grenfell, and Tony Worby for discussions. Cloud observations were

obtained from the Comprehensive Ocean–Atmosphere Data Set (COADS) provided by the U.S. National Center for Atmospheric Research and the U.S. National Oceanic and Atmospheric Administration; Scott Woodruff provided assistance in accessing these data. Cloud observations archived by the Commonwealth Bureau of Meteorology were also used; we thank Ian Barnes-Keoghan and Doug Shepherd. Sea ice observations were obtained from the Australian Antarctic Division Data Centre as part of the Antarctic Sea Ice Processes and Climate (ASPeCt) program; Jono Reeve and Peter Wiley provided invaluable help. This work was supported by NSF Grants OPP-95-27244 and OPP-98-15156, and by a NASA Earth System Science Fellowship to Melanie Fitzpatrick. We also thank two anonymous reviewers for helpful comments that improved the clarity of our paper.

REFERENCES

Allison, I., R. E. Brandt, and S. G. Warren, 1993: East Antarctic sea ice: Albedo, thickness distribution, and snow cover. *J. Geophys. Res.,* **98,** 12 417–12 429.

Ambrosetti, P., H. E. B. Anderson, L. Liedquist, C. Fröhlich, C. Wehrli, and H. D. Talarek, 1986: Results of an outdoor and indoor pyranometer comparison. International Energy Agency Solar Heating and Cooling Program Rep., World Radiation Center, Davos, Switzerland, 211 pp.

Ayers, G. P., and J. L. Gras, 1991: Seasonal relationship between cloud condensation nuclei and aerosol methane sulphonate in marine air. *Nature,* **353,** 834–835.

Barker, H. W., T. J. Curtis, E. Leontieva, and K. Stamnes, 1998: Optical depth of overcast cloud across Canada: Estimates based on surface pyranometer and satellite measurements. *J. Climate,* **11,** 2980–2994.

Boers, R., and P. B. Krummel, 1998: Microphysical properties of boundary layer clouds over the Southern Ocean during ACE 1. *J. Geophys. Res.,* **103,** 16 651–16 663.

——, A. van Lammeren, and A. Feijt, 2000: Accuracy of cloud optical depth retrievals from ground-based pyranometers. *J. Atmos. Oceanic Technol.,* **17,** 916–927.

Brandt, R. E., S. G. Warren, A. P. Worby, and T. C. Grenfell, 2005: Surface albedo of the Antarctic sea ice zone. *J. Climate,* **18,** 3606–3622.

Fitzpatrick, M. F., R. E. Brandt, and S. G. Warren, 2004: Transmission of solar radiation by clouds over snow and ice surfaces: A parameterization in terms of optical depth, solar zenith angle, and surface albedo. *J. Climate,* **17,** 266–275.

Hahn, C. J., S. G. Warren, and J. London, 1995: The effect of moonlight on observation of cloud cover at night, and application to cloud climatology. *J. Climate,* **8,** 1429–1446.

Henderson-Sellers, A., and K. McGuffie, 1988: A quantitative evaluation of surface-based observations of oceanic cloudiness. *Atmos. Res.,* **21,** 241–260.

Leontyeva, E., and K. Stamnes, 1994: Estimations of cloud optical thickness from ground-based measurements of incoming solar radiation in the Arctic. *J. Climate,* **7,** 566–578.

Lubin, D., and A. S. Simpson, 1997: Measurement of surface radiation fluxes and cloud optical properties during the 1994 Arctic Ocean Section. *J. Geophys. Res.,* **102,** 4275–4286.

Mahesh, A., V. P. Walden, and S. G. Warren, 2001: Ground-based infrared remote sensing of cloud properties over the Antarctic Plateau. Part II: Cloud optical depths and particle sizes. *J. Appl. Meteor.,* **40,** 1279–1294.

Minnett, P. J., 1999: The influence of solar zenith angle and cloud type on cloud radiative forcing at the surface in the Arctic. *J. Climate,* **12,** 147–158.

Nichol, S. E., G. Pfister, G. E. Bodecker, R. L. McKenzie, S. W. Wood, and G. Bernhard, 2003: Moderation of cloud reduction of UV in the Antarctic due to high surface albedo. *J. Appl. Meteor.,* **42,** 1174–1183.

Pfister, G., R. L. McKenzie, J. B. Liley, A. Thomas, B. W. Forgan, and C. N. Long, 2003: Cloud coverage based on all-sky imaging and its impact on surface solar irradiance. *J. Appl. Meteor.,* **42,** 1421–1434.

Press, W. H., S. A. Teukolsky, W. T. Vetterling, and B. P. Flannery, 1992: *Numerical Recipes in C: The Art of Scientific Computing*. Cambridge University Press, 994 pp.

Ricchiazzi, P., C. Gautier, and D. Lubin, 1995: Cloud scattering optical depth and local surface albedo in the Antarctic: Simultaneous retrieval using ground-based radiometry. *J. Geophys. Res.,* **100,** 21 091–21 104.

Rogers, R. R., 1979: *A Short Course in Cloud Physics.* Pergamon Press, 235 pp.

van Loon, H., 1972: Clouds and precipitation in the Southern Hemisphere. *Meteorology of the Southern Hemisphere*, *Meteor. Monogr.*, No. 37, Amer. Meteor. Soc., 101–111.

Warren, S. G., C. J. Hahn, J. London, R. M. Chervin, and R. L. Jenne, 1988: Global distribution of total cloud cover and cloud type amounts over the ocean. NCAR Tech. Note TN-317+STR, Boulder, CO, 42 pp. + 170 maps.

Wiscombe, W. J., 1975: Solar radiation calculations for Arctic summer stratus conditions. *Climate of the Arctic,* G. Weller and S. A. Bowling, Eds., University of Alaska Press, 245–254.

WMO, 1956: *International Cloud Atlas.* World Meteorological Organization, Geneva, Switzerland, 62 pp. + 72 plates.

Woodruff, S. D., H. F. Diaz, J. D. Elms, and S. J. Worley, 1998: COADS release 2 data and metadata enhancements for improvements of marine surface flux fields. *Phys. Chem. Earth,* **23,** 517–527.

Worby, A. P., 1999: *Observing Antarctic Sea Ice: A Practical Guide for Conducting Sea-Ice Observations from Vessels Operating in the Antarctic Pack Ice.* ASPECT/SCAR/GLOCHANT program, Australian Antarctic Division, Hobart, Australia, CD-ROM.